Extensive Molecular Dynamics Simulations Showing That Canonical G8 and Protonated A38H$^+$ Forms Are Most Consistent with Crystal Structures of Hairpin Ribozyme

Vojtěch Mlýnský,[†] Pavel Banáš,[†,‡] Daniel Hollas,[†] Kamila Réblová,[‡] Nils G. Walter,[§] Jiří Šponer,*[,†,‡] and Michal Otyepka*[,†,‡]

Department of Physical Chemistry, Faculty of Science, Palacky University Olomouc, tr. 17. listopadu 12, 771 46 Olomouc, Czech Republic, Institute of Biophysics, Academy of Sciences of the Czech Republic, Kralovopolska 135, 612 65 Brno, Czech Republic, and Department of Chemistry, Single Molecule Analysis Group, University of Michigan, 930 North University Avenue, Ann Arbor, Michigan 48109-1055

Received: January 6, 2010; Revised Manuscript Received: April 12, 2010

The hairpin ribozyme is a prominent member of the group of small catalytic RNAs (RNA enzymes or ribozymes) because it does not require metal ions to achieve catalysis. Biochemical and structural data have implicated guanine 8 (G8) and adenine 38 (A38) as catalytic participants in cleavage and ligation catalyzed by the hairpin ribozyme, yet their exact role in catalysis remains disputed. To gain insight into dynamics in the active site of a minimal self-cleaving hairpin ribozyme, we have performed extensive classical, explicit-solvent molecular dynamics (MD) simulations on time scales of 50−150 ns. Starting from the available X-ray crystal structures, we investigated the structural impact of the protonation states of G8 and A38, and the inactivating A-1(2′-methoxy) substitution employed in crystallography. Our simulations reveal that a canonical G8 agrees well with the crystal structures while a deprotonated G8 profoundly distorts the active site. Thus MD simulations do not support a straightforward participation of the deprotonated G8 in catalysis. By comparison, the G8 enol tautomer is structurally well tolerated, causing only local rearrangements in the active site. Furthermore, a protonated A38H$^+$ is more consistent with the crystallography data than a canonical A38. The simulations thus support the notion that A38H$^+$ is the dominant form in the crystals, grown at pH 6. In most simulations, the canonical A38 departs from the scissile phosphate and substantially perturbs the structures of the active site and S-turn. Yet, we occasionally also observe formation of a stable A-1(2′-OH)···A38(N1) hydrogen bond, which documents the ability of the ribozyme to form this hydrogen bond, consistent with a potential role of A38 as general base catalyst. The presence of this hydrogen bond is, however, incompatible with the expected in-line attack angle necessary for self-cleavage, requiring a rapid transition of the deprotonated 2′-oxyanion to a position more favorable for in-line attack after proton transfer from A-1(2′-OH) to A38(N1). The simulations revealed a potential force field artifact, occasional but irreversible formation of "ladder-like", underwound A-RNA structure in one of the external helices. Although it does not affect the catalytic center of the hairpin ribozyme, further studies are under way to better assess possible influence of such force field behavior on long RNA simulations.

Introduction

The hairpin ribozyme is a self-cleaving and -ligating catalytic RNA motif classified as a small RNA enzyme or ribozyme (Figure 1). It is found in the minus strand of the satellite RNA associated with the *Tobacco Ringspot Virus*, where it promotes double-rolling circle replication.[1−3] It can also be engineered to catalyze reversible, site-specific phosphodiester bond cleavage on an external, complementary RNA substrate.[4] The hairpin ribozyme achieves rate acceleration similar to that for other ribozymes,[5,6] and it does not require a specific metal ion to achieve full catalytic efficiency (cleavage rate ∼0.5 min^{-1}).[4,7] Although the folded hairpin ribozyme features an active site pocket of deep negative potential, similar to that of the hepatitis delta virus (HDV) ribozyme, once formed, this pocket appears to be secluded from solvent,[8] in sharp contrast to the open pocket of the HDV ribozyme.[9] The HDV ribozyme catalytic pocket is known to interact with divalent ions. If divalents are not present, the pocket is immediately (in molecular dynamics simulations on nanoseconds time scale)[9,10] soaked by monovalent ions that are likely to interfere with the deep negative potential. The hairpin ribozyme, as it avoids interactions with ions sterically, is thus exposing RNA functional groups and water molecules in the active site to a largely uncompensated negative electrostatic potential for long time periods. Previous molecular dynamics (MD) simulations suggested that long-residency water molecules in the active site may thus become activated to participate in catalysis.[8,11−13] The established lack of a catalytic metal ion requirement makes the hairpin ribozyme an especially useful model system in which to probe the direct role of nucleobases in RNA catalysis as a major remaining challenge in the field.[14]

A range of structural and biochemical data have implicated guanine 8 (G8) and adenine 38 (A38) as direct participants in catalysis of cleavage and ligation (Figure 2). Mutation or deletion of the conserved G8 in loop A near the scissile phosphate diminishes activity by ∼1000-fold without signifi-

* Corresponding authors. M.O.: tel, +420 585 634 756; fax, +420 585 634 761; e-mail, michal.otyepka@upol.cz, J.S.: tel, +420 541 517 133; e-mail, sponer@ncbr.chemi.muni.cz.
[†] Palacky University Olomouc.
[‡] Academy of Sciences of the Czech Republic.
[§] University of Michigan.

10.1021/jp1001258
Published on Web 04/26/2010

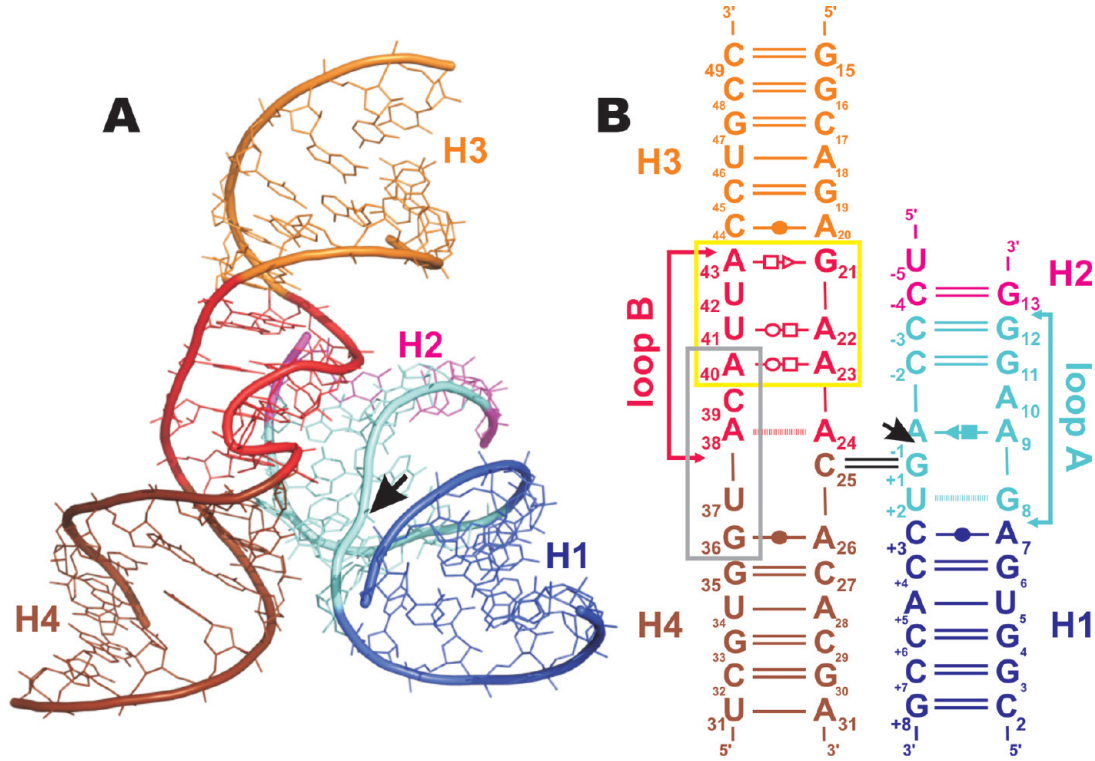

Figure 1. Structure of the junction-less hairpin ribozyme. (A) Three-dimensional structure of the hairpin ribozyme, the double helical A-RNA stems (H1−H4) and loops are shown in different colors. The black arrow indicates the cleavage site. (B) Sequence and secondary structure of the hairpin ribozyme. The colors of helical stems and loops match those in panel A. S-turn and E-loop motifs in loop B are indicated by gray and yellow boxes, respectively. Base pairs are annotated using standard classification.[72] The black arrow indicates the cleavage site.

cantly disrupting the global structure of the ribozyme.[15−17] The position of G8 near the 2′-OH attacking nucleophile, as observed in crystal structures, first suggested the possibility that an N1 unprotonated G8$^-$ may act as general base during catalysis (Figure 2A).[11,15,18,19] Recent experiments measuring the ionization state of an 8-azaguanosine substitution at this position, however, do not provide support for the G8$^-$ general base mechanism as the pK_a of G8 was estimated to be 9.5,[20] near the unperturbed pK_a value of guanine, making deprotonation unlikely.[21] Exogenous nucleobase rescue experiments suggested that the catalytic role of G8 rather lies in charge stabilization of the transition state (TS) and/or alignment of the reactive groups.[13,14,16,22] Recent molecular dynamics (MD) and quantum mechanical/molecular mechanical (QM/MM) calculations are consistent with the latter model, as they suggest that G8 could facilitate catalysis through stabilizing both the developing charge on the scissile phosphate and the strained backbone conformations adopted along the reaction pathway.[23−25] A direct comparison as to what extent the two possible G8 protonation states are structurally compatible with the crystal structures is still lacking.

Compared to that case for G8, a substantially stronger inhibition is affected by abasic substitution of A38, which impairs catalysis more than 10 000-fold. Furthermore, exogenous nucleobase rescue experiments indicate that the protonation state of A38(N1) plays a direct role in catalysis.[26,27] Crystal structures of TS analogs place A38(N1) near the 5′-oxygen leaving group, implicating A38 as the general acid.[19,28−30] In accordance, recent crystallographic and molecular dynamics studies support involvement of the A38(N1) imino group in catalysis.[23,31] Raman spectroscopy shows that the pK_a of A38 is shifted toward neutrality, implying that A38 might be protonated under physiological pH ∼7 prior to cleavage.[32] This shift in pK_a and the resulting protonation of A38 is expected to be facilitated by the pocket of negative electrostatic potential in the solvent-shielded active site.[8,32] An alternative role of A38 in alignment of reactive groups and electrostatic stabilization of negative charge in the TS was also suggested.[23,26,27] A possible involvement of A38 in catalysis has been studied by QM/MM, with the conclusion that two mechanisms are plausible involving either A38 in electrostatic stabilization of the TS or the protonated A38H$^+$ in general acid catalysis (Figure 2B).[24,25] Finally, on the basis of recent MD simulations a third reaction mechanism has been suggested, where A38 acts as a proton shuttle (Figure 2C).[23]

Despite all experimental and computational efforts, a consensus on the protonation states and catalytic roles of G8 and A38 has not been reached.[6] In the present study, we use classical MD simulations on 50−150 ns time scales (more than 1.1 μs in total, as summarized in Table 1) to explicitly address the protonation states of G8 and A38 prior to cleavage. Our results suggest that the crystal structures most likely harbor a canonical G8 (or possibly the G8 enol tautomer) and a protonated A38H$^+$. Additionally, we document in detail the marked structural impact on active site architecture that a catalysis-blocking A-1(2′-methoxy) modification has, often used for convenient crystallization.

Molecular Dynamics

Starting structures of a minimal, junction-less hairpin ribozyme for MD simulations (Table 1) were derived from a crystal structure grown at 6.0 pH and determined at (2.05 Å) resolution (PDB code 2OUE, original PDB code 1ZFR).[11] The simulated systems were neutralized with Na$^+$ counterions and immersed in a rectangular water box with an at least 10.0 Å thick layer of TIP3P water molecules all around the RNA solute. The solute−solvent system was minimized prior to MD simulation as follows. Minimization of the ribozyme hydrogen atoms

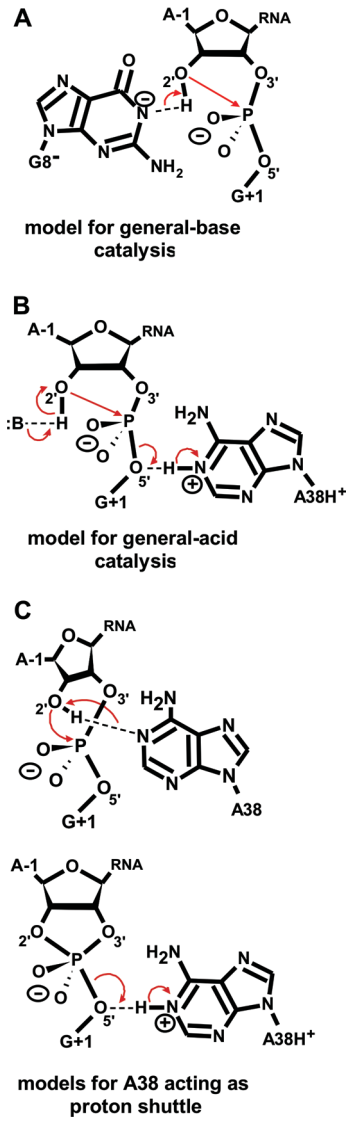

Figure 2. Three catalytic strategies proposed for phosphodiester cleavage by the hairpin ribozyme. (A) Mechanism with $G8^-$ as the general base accepting a proton from the A-1(2′-OH) nucleophile. (B) Mechanism in which $A38H^+$ acts as the general acid protonating the leaving G+1(O5′) alcoholate. (C) Mechanism in which A38 acts as a proton shuttle accepting a proton from the A-1(2′-OH) nucleophile and transferring it to the leaving group G+1(O5′).

TABLE 1: Overview of Performed MD Simulations

simulation label	A-1	G8	A38	time (ns)	force field
WT/G8$^-$/A38	2′-OH	G8$^-$	A38	74	Parm99
WT/G8$^-$/A38H$^+$	2′-OH	G8$^-$	A38H$^+$	50	Parm99
WT/G8t/A38	2′-OH	G8t[b]	A38	66	Parm99
WT/G8t/A38H$^+$	2′-OH	G8t[b]	A38H$^+$	69	Parm99
OMe/G8/A38	2′-OMe[a]	G8	A38	50	Parm99
OMe/G8/A38H$^+$	2′-OMe	G8	A38H$^+$	100	Parm99
WT1/G8/A38	2′-OH	G8	A38	50	Parm99
WT2/G8/A38	2′-OH	G8	A38	150	Parm99
WT1/G8/A38H$^+$	2′-OH	G8	A38H$^+$	50	Parm99
WT2/G8/A38H$^+$	2′-OH	G8	A38H$^+$	150	Parm99
WT/G8/A38/ES	2′-OH	G8	A38	80[c]	Parm99
WT/G8/A38H$^+$/ES	2′-OH	G8	A38H$^+$	80[c]	Parm99
WT/G8/A38/bsc0	2′-OH	G8	A38	150	Parmbsc0
WT/G8/A38H$^+$/bsc0	2′-OH	G8	A38H$^+$	150	Parmbsc0

[a] 2′-OMe stands for 2′-methoxy. [b] G8t stands for guanine-*N*1,*O*6-enol tautomer. [c] Simulation with excess salt (KCl).

was followed by minimization of counterions and water molecules. Subsequently, the ribozyme was frozen and solvent molecules with counterions were allowed to move during a 10 ps long MD run to relax the density in the box. The nucleobases were allowed to relax in several minimization runs with decreasing force constants applied to the backbone phosphate atoms. After full relaxation, the system was slowly heated to 298.15 K over 100 ps using 2 fs time steps and *NpT* conditions. The simulations were performed under periodic boundary conditions in the *NpT* ensemble (298.15 K, 1 atm) with 2 fs time steps. The particle-mesh Ewald method was used to calculate electrostatic interactions and a 10.0 Å cutoff was applied for Lennard-Jones interactions. The SHAKE algorithm was applied to all bonds containing hydrogen atoms. The SANDER module of AMBER 9.0[33] with the Cornell et al. force field parm99[34] was used for all simulations, except for two reference MD simulations (Table 1) where instead the recent parmbsc0 version[35] of the Cornell et al. force field was used. Two additional MD simulations (marked as "ES" in Table 1) were run in KCl salt excess with a 10.0 Å thick layer of SPC/E water molecules (parameters for KCl were taken from ref 36). The parameters for all nonstandard residues (Supporting Information) were derived according to the Cornell et al. procedure.[37] Partial atomic charges were determined using restrained electrostatic potential (RESP) fits.[38] The ab initio calculations required for the parametrization of the protonated adenine, 2′-methoxy-adenine, deprotonated guanine, and guanine-*N*1,*O*6-enol tautomer were carried out using the Gaussian03 program[39] at the HF/6-31G(d) level of theory (see Supporting Information for details of this parametrization).

Results

O2′-Methoxy Group of A-1 Distorts the Active Site of the Hairpin Ribozyme. The 2′-methoxy modification of the active site A-1 nucleotide was recently used by Wedekind and coworkers to solve the crystal structure of a minimal hairpin ribozyme in a precleavage state at the highest resolution obtained for this ribozyme yet, 2.05 Å[11] (see a recent review[6] for a summary of all crystal structures of the hairpin ribozyme). Previous MD studies and recent X-ray crystallography data suggested that this 2′-methoxy group distorts the conformation of the A-1 nucleotide,[8,23,31] but so far no MD simulation including this modification has emerged. Thus we compared two simulations with the catalytically inactivating 2′-methoxy group at A-1 (denoted as OMe simulations, one with a canonical A38, labeled as OMe/G8/A38, and the other with a protonated $A38H^+$, labeled as OMe/G8/A38H$^+$; see Table 1) alongside corresponding simulations carrying the native 2′-hydroxyl group (labeled as WT simulations; see Table 1).

Among all OMe and WT simulations, the lowest root-mean-square deviation (rmsd) of the active site from that in the crystal structure was observed in the OMe/G8/A38H$^+$ simulation with an rmsd of 1.07 Å (average 49−50 ns into the simulation), suggesting that this simulation is in best agreement with the crystallographic geometry (Supporting Information Figure S9).

We observed that the 2′-methoxy group of A-1 remained stable in its crystallographic position (Figure 3A) in both OMe simulations (OMe/G8/A38 and OMe/G8/A38H$^+$). Most notably, the sugar moiety of the 2′-methoxylated A-1 preserved its crystallographic C2′-endo sugar pucker, whereas the G8(N1H) (occasionally alternating with G8(N2H) in the OMe/G8/A38H$^+$ simulation) remained in hydrogen bonding contact with the oxygen of the 2′-methoxy group (Figure 3D). A slight adjustment of the scissile phosphate was the only deviation in the structural arrangement of the A-1 and G+1 nucleotides with respect to the crystal structure, which occurred in both OMe

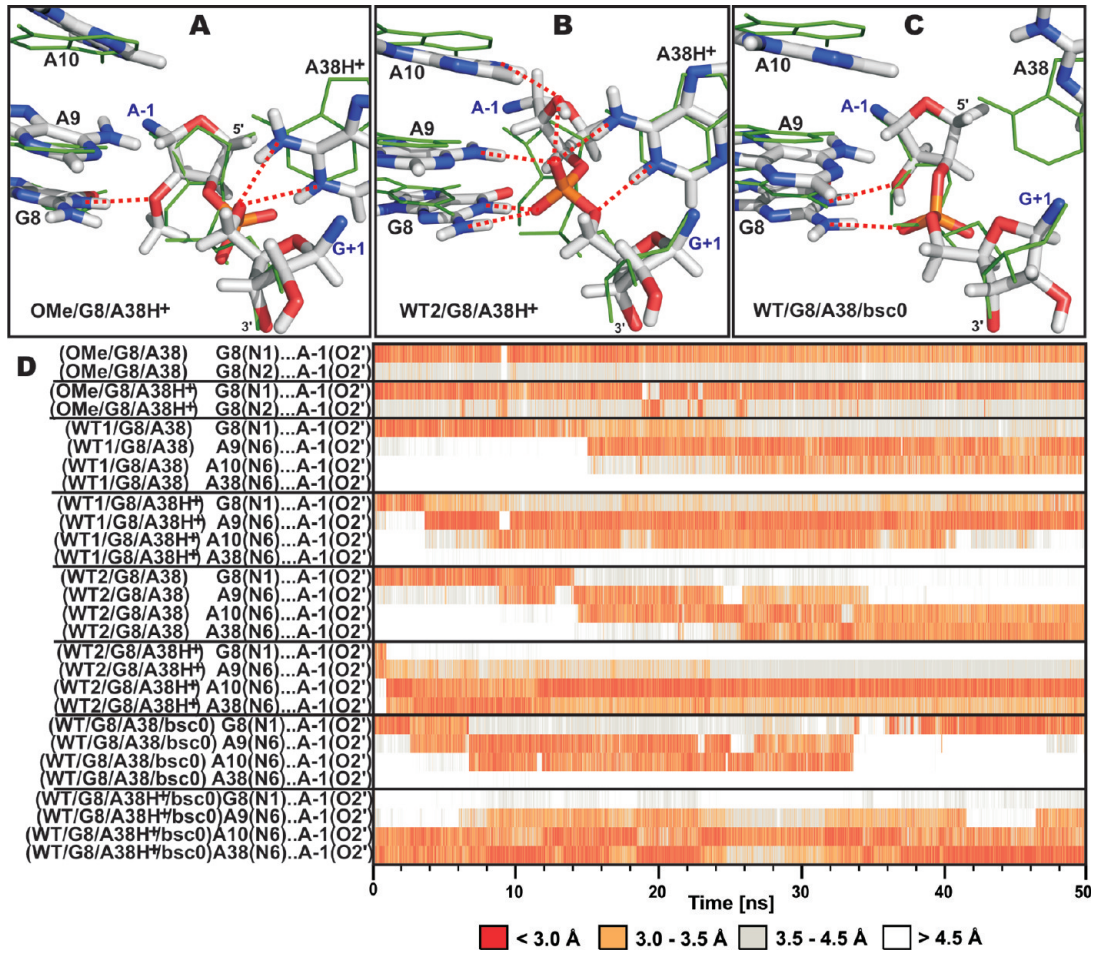

Figure 3. Active site structures of MD simulations with either a 2′-methoxy or 2′-OH moiety on A-1 and distinct A38 protonation states. (A) Simulation OMe/G8/A38H$^+$ retains a crystal structure like arrangement of the active site, which is different from the dominant architecture observed with the native cleavage site A-1(2′-OH). (B) Simulation WT2/G8/A38H$^+$ illustrates repuckering of the A-1 sugar upon introduction of the native A-1(2′-OH). (C) Simulation WT/G8/A38/bsc0 shows a reversible flip-flop of the native A-1(2′-OH) between 2′-endo and 2′-exo. The structures shown (sticks) are averaged over the last nanosecond of the simulation and superimposed (on the basis of the A-1 and G+1 nucleobases) with the starting crystal structure (green lines). Red dashed lines indicate key hydrogen bonds within the active site. (D) Time evolution of hydrogen bonds (the color scale is preserved throughout) involving the A-1(O2′) oxygen over the course of the indicated MD simulations. For clarity, only the first 50 ns of each simulation is shown; however, we note that the arrangement of the active site remains intact in all simulations after these 50 ns.

simulations (~7.5 ns into the OMe/G8/A38H$^+$ and ~1.0 ns into the OMe/G8/A38 simulation; see Figure 3A). This flip of the scissile phosphate was induced by a change in the A-1 backbone torsion ε from 150° to 80° and resulted in loss of the hydrogen bond between G8(N2H) and the G+1(*pro*-R_P) nonbridging phosphate oxygen (see Supporting Information Figure S2 for an annotated architecture of the active site in the crystal structure with the IUPAC terminology of the *pro*-R_P/S_P nonbridging phosphate oxygens). In addition, a departure of A38 from the active site geometry was observed in the OMe/G8/A38 simulation that includes a canonical A38 and is discussed more thoroughly below. Taken together, the OMe/G8/A38H$^+$ simulation agrees well with the crystal structure except for the above-mentioned slight shift of the scissile phosphate, which may well represent an artifact caused by inaccuracies of the empirical force field.[40]

In contrast, introduction of the native A-1(2′-OH) sugar moiety in the WT led to significant reconfiguration of the active site within the first 20 ns of all resulting simulations. The A-1 sugar pucker flipped from the original C2′-endo/C3′-exo to C2′-exo/C3′-endo; this flip was always accompanied by a shift of the A-1(2′-OH) group from above the G8 base plane toward the A38 Watson−Crick (WC) edge (Figure 3B). As a consequence, the A-1(2′-OH) group made hydrogen bonds either with A9(N6H) and A10(N6H) (in simulations WT1/G8/A38, WT1/G8/A38H$^+$, WT/G8$^-$/A38, WT/G8t/A38, and WT/G8/A38/bsc0) or with A38/A38H$^+$(N6H) (observed in simulations WT2/G8/A38, WT2/G8/A38H$^+$, WT/G8/A38H$^+$/bsc0, WT/G8/A38/ES, WT/G8/A38H$^+$/ES, WT/G8$^-$/A38H$^+$, and WT/G8t/A38H$^+$). Such a behavior of the native A-1(2′-OH) group has also been noted in recent MD simulations[23] and crystal structures.[31] Notably, the shift of the A-1(2′-OH) group was more rapid in simulations with protonated A38H$^+$ than in simulations with canonical A38. In one case (~34 ns into the WT/G8/A38/bsc0 simulation with the parmbsc0 force field, Figure 3C), the A-1(2′-OH) group flipped back to a C2′-endo conformation resembling that of the 2′-methoxy group so that both the G8(N1H)···A-1(O2′) and the G8(N2H)···G+1(*pro*-R_P) hydrogen bonds[11] were restored (Figure 3D, Supporting Information Figures S2A and S3B and Table S2). Since the feasible simulation time scale is still far from full convergence, we are presently not able to determine whether this difference is caused by the parmbsc0 force field or is coincidental.[40] Considering all available current and past simulations, however, there is strong evidence that the active site is distorted by the crystallographic 2′-methoxy modification.

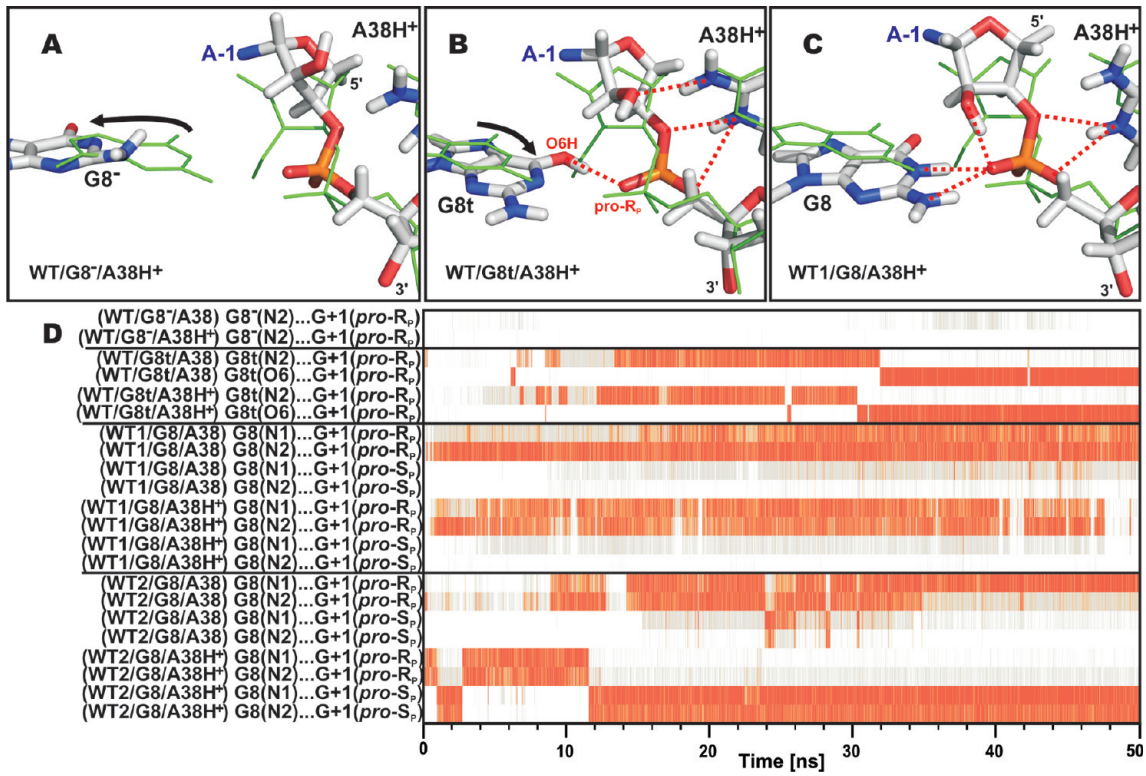

Figure 4. Active site structures of MD simulations with distinct G8 (and A38) protonation states. (A) Simulation WT/G8$^-$/A38H$^+$, where G8$^-$ leaves the proximity of the scissile phosphate (black arrow). (B) Simulation WT/G8t/A38H$^+$ documents a contact between G8t and the scissile phosphate with a G8t(O6H)···G+1(*pro*-R$_P$) hydrogen bond re-formed after an initial expulsion of G8t (black arrow). (C) Simulation WT1/G8/A38H$^+$ shows the typical G8···G+1 4BPh contact in simulations with a canonical G8. The structures shown (sticks) are averaged over the last nanosecond of the simulation and superimposed (on the basis of the A-1 and G+1 nucleobases) with the starting crystal structure (green lines). (D) Time evolution of interatomic distances (the color scale is the same as in Figure 3) between G8 and the G+1 *pro*-R$_P$ and *pro*-S$_P$ oxygen atoms during the first 50 ns of each MD simulation.

Canonical Form of G8 Is Consistent with the Crystal Structure. We carried out a set of simulations to compare the structural dynamics of three possible protonation states of G8, i.e., the canonical guanine (G8), the N1,O6-enol tautomer (G8t), and the N1-deprotonated form (G8$^-$), in the presence of the native A-1(2′-OH) group (Table 1; see Supporting Information Figure S1 for the structures of the G8 protonation forms). It is worth noting that the protonation state of G8 influenced both A38 and A38H$^+$ simulations similarly. Likewise, the A-1 sugar repuckering induced by A-1(2′-OH) described in the previous paragraph was observed in all simulations independent of the G8 protonation state.

Both simulations carrying the deprotonated G8$^-$ form (i.e., WT/G8$^-$/A38 and WT/G8$^-$/A38H$^+$) showed expulsion of the G8$^-$ from the active site during the initial equilibration. Both the G8(N2H)···G+1(*pro*-R$_P$) and the G8(N1)···A-1(2′-OH) hydrogen bonds observed in the crystal structure were disrupted and not reestablished over the entire simulation (Figure 4A,D). A similar expulsion of the G8 nucleobase occurred during the equilibration of both simulations with the G8t tautomer (WT/G8t/A38 and WT/G8t/A38H$^+$); however, G8 returned to its original position in the active site during the first 10 ns in both simulations and reestablished the G8t(N2H)···G+1(*pro*-R$_P$) hydrogen bond (Figure 4D). This G8t(N2H)···G+1(*pro*-R$_P$) hydrogen bond was finally disrupted and immediately replaced by a newly formed G8t(O6H)···G+1(*pro*-R$_P$) hydrogen bond 30−35 ns into both simulations, which remained a stable binding pattern of G8t to the scissile phosphate over the rest of the simulations (Figure 4B,D). Therefore, while G8t causes a local, minor rearrangement of the active site compared to the crystal structure, it remained quite compatible with the overall hairpin ribozyme structure.

By comparison, G8 stayed in more stable contact with the scissile phosphate in all simulations harboring the canonical G8 form (i.e., WT1/G8/A38, WT2/G8/A38, WT1/G8/A38H$^+$, and WT2/G8/A38H$^+$; Figure 4D), making base-phosphate (BPh)[41] contacts to the G+1(*pro*-R$_P$) or (*pro*-S$_P$) nonbridging oxygens. These BPh interactions between G8 and the scissile phosphate fluctuated among 3BPh, 4BPh, and 5BPh binding patterns (Figure 4C,D).[41] The 5BPh contact of G8 to the G+1(*pro*-R$_P$) nonbridging oxygen was accompanied by a G8(N1H)···A-1(O2′) hydrogen bond in simulation WT/G8/A38/bsc0. This distinct arrangement was caused by the reversion of the C2′-endo-to-C3′-endo repuckering induced by the native A-1(2′-OH) and discussed above (see Figure 3C).

Protonated A38H$^+$, but Not A38, Is Consistent with the Crystal Structure. We observed significant differences in the behavior of canonical A38 and protonated A38H$^+$ forms. The protonated A38H$^+$ remained tightly bound in its crystal-like position in the active site, while the canonical A38 form was expelled from the active site. The A38H$^+$(N1)···G+1(O5′) hydrogen bond, which has been suggested to play a key role in catalysis,[18,19,23,28−30] remained stable in all simulations carrying the protonated form of A38H$^+$ (Figure 5D). Note that OMe/G8/A38H$^+$ is the only simulation where the A38H$^+$(N1H)···G+1(O5′) contact was temporarily interrupted and departure of A38H$^+$ from the scissile phosphate occurred. However, a return of A38H$^+$ and subsequent restoration of the A38H$^+$(N1H)···G+1(O5′) hydrogen bond was observed ∼36 ns into this simulation (Figure 5D).

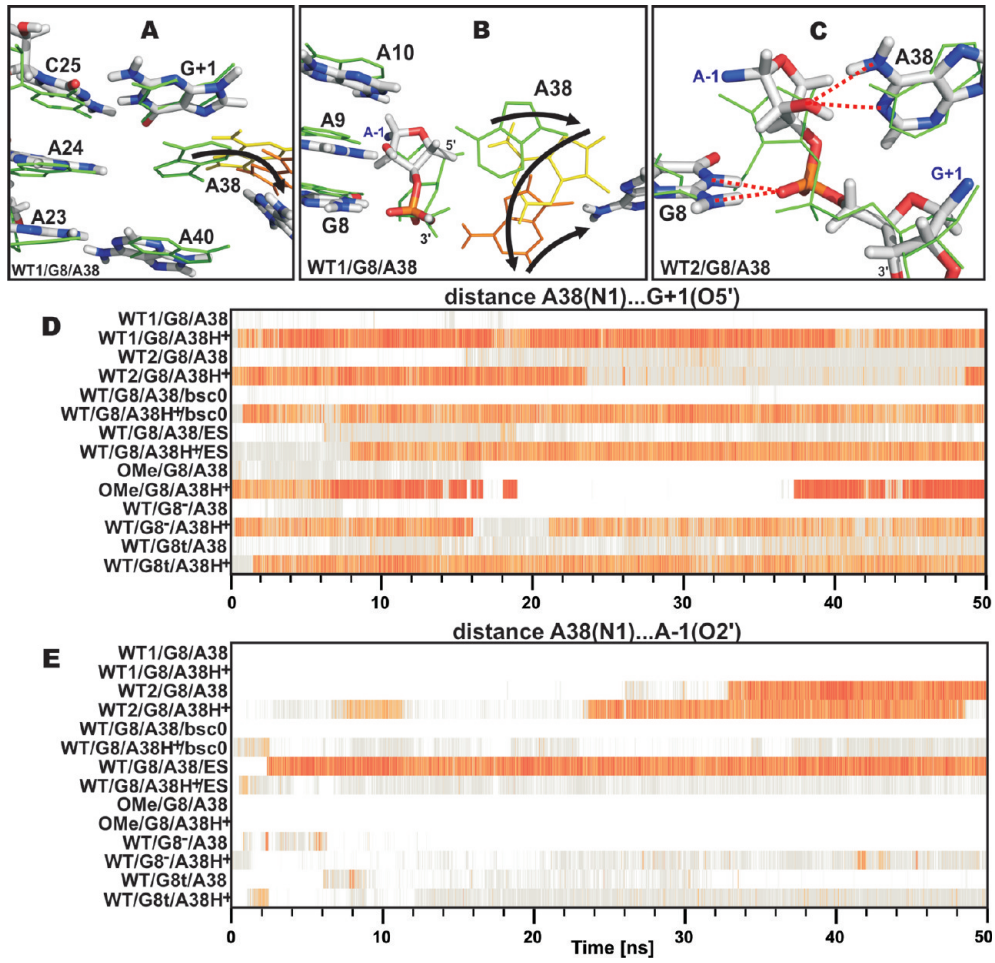

Figure 5. Canonical A38 either loses pairing with the A24 nucleobase while leaving the active site during the majority of MD simulations or, alternatively, establishes an A-1(2′-OH)···A38(N1) hydrogen bond. (A) Stick representation of the average structure of the last nanosecond of simulation WT1/G8/A38 illustrating the A38-A24 base pair disruption. While the crystal geometry is represented by green lines, yellow and orange lines represent snapshots of consecutive A38 positions during its expulsion (black arrow) from the active site. (B) Same as panel A, but from a different viewpoint. (C) Average structure of the active site (taken from the last nanosecond of simulation WT2/G8/A38 and overlaid with the crystal structure in green) showing A38(N6H)···A-1(O2′) and A-1(2′-OH)···A38(N1) hydrogen bond formation. (D) and (E) Time evolution of the A38(N1)···G+1(O5′) and A38(N1)···A-1(O2′) distances in all simulations.

In sharp contrast to the protonated A38H$^+$, the canonical A38 typically shifted away from the scissile phosphate; the distance between A38(N1) and G+1(O5′) gradually increased up to 7−8 Å, the pairing with A24 was interrupted and, eventually, A38 left the active site in simulations WT1/G8/A38, OMe/G8/A38, WT/G8/A38/bsc0, WT/G8t/A38 and WT/G8$^-$/A38 (Figure 5A,B,D). Alternatively, in simulations WT2/G8/A38 and WT/G8/A38/ES the A38(N1)···G+1(O5′) distance similarly increased to 5 Å, but then A38 established an A38(N6H)···A-1(O2′) hydrogen bond (in WT2/G8/A38 at ∼26 ns and in WT/G8/A38/ES simulation at ∼2 ns, Supporting Information Figure S3A), which was followed by A-1(2′-OH)···A38(N1) hydrogen bond formation (in WT2/G8/A38 at ∼34 ns and in WT/G8/A38/ES simulation at ∼2 ns; Figure 5C,E). The A-1(2′-OH)···A38(N1) hydrogen bond remained stable until the end of both simulations (Supporting Information Figure S3B). The formation of this A-1(2′-OH)···A38(N1) hydrogen bond corresponds to the recently described interaction between A-1(2′-OH) and A38(N1), which was suggested to be catalytically relevant (Figure 2C).[23] Notably, the formation of the A-1(2′-OH)···A38(N1) hydrogen bond was inevitably accompanied by a loss of the O2′−P−O5′ in-line attack configuration involving A-1(2′-OH) (Supporting Information Figure S4A).

To further validate the observed differences in A38 and A38H$^+$ behavior, we performed two additional, 150-ns-long MD simulations of the hairpin ribozyme with native A-1(2′-OH) and parmbsc0 force field and two 80-ns-long MD simulations with excess KCl salt, in both cases one simulation with a canonical A38, the other with protonated A38H$^+$. Parmbsc0 is the latest variant of the parm99 force field, which features modified α/γ torsion profiles that suppress γ-trans geometries.[35] Parmbsc0 leads to a decisive improvement of B-DNA simulations,[35,42,43] while both force fields seem to perform equally well for RNA simulations.[35,44−48] In the excess salt simulations we replaced the Na$^+$ counterions by twice the amount of K$^+$ ions and Cl$^-$ ions for charge neutralization. Net neutralization results in a sodium concentration of ∼0.30 M, while the latter simulations contain ∼0.65 M K$^+$. Such excess KCl salt conditions in MD simulations were recently shown to cause a modest sequence-dependent compaction of canonical A-RNA double helices.[48] Significantly, the distinct behavior of A38 and A38H$^+$ simulations was reproduced with both the parm99 and parmbsc0 force field as well as in the presence of neutralizing Na$^+$ counterions and excess KCl salt. We conclude that the compact binding of the protonated A38H$^+$ to G+1(O5′), the expulsion of the canonical A38 from the active site, and the alternative, less common shift of A38 toward the A-1(2′-OH) are robust results reflective of the A38 protonation state and independent of other details of the MD simulation.

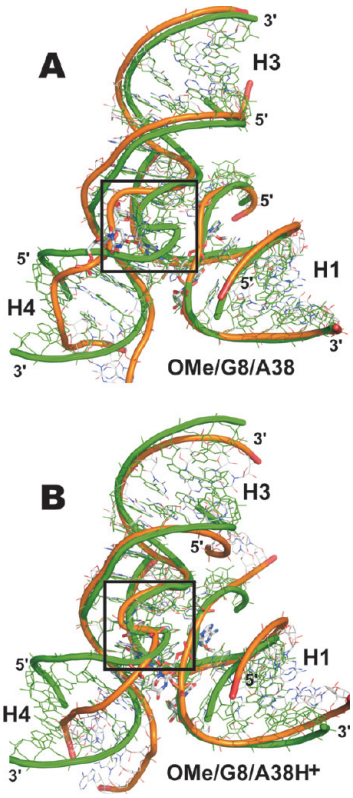

Figure 6. Ribbon diagrams showing the average structures from the last nanosecond (orange ribbon) superimposed over the crystal structure (green) of the minimal junction-less hairpin ribozyme with helixes H1−H4 indicated. (A) Simulations with canonical A38 (here OMe/G8/A38) show S-turn degradation (black box). (B) Simulations with protonated A38H$^+$ (here OMe/G8/A38H$^+$) preserve the crystallographic S-turn conformation.

S-Turn Behavior. The crystal structures suggest that BPh contacts may contribute to the stability of the S-turn region located between helices H3 and H4 (Figure 1). Accordingly, we observed a strong correlation between S-turn behavior and the presence of the BPh contact between A38(N1) and G+1(O5′). This interaction, which places the A38(N1) atom within 2.6−2.8 Å of G+1(O5′) and is also observed in the oxo-vanadium TS-mimic X-ray structures,[19,28] is very unique since it does not correspond to any established BPh interaction pattern as classified by Zirbel et al.[41] In fact, there are no more than two candidates for such an interaction found in the available ribosomal structures and even these cases may be artificial due to resolution limits.[41] Since the relative orientation of A38 with respect to the G+1 phosphate closely mimics the 4BPh interaction of guanine-phosphate, where the N1 nitrogen of guanine is protonated, this unique arrangement of A38···G+1 provides a very strong indication that the adenine A38 is protonated in the crystal structure, which was grown at pH 6. As discussed above, we observed this unique 4BPh interaction between A38H$^+$ and G+1 phosphate to be stable in all MD simulations carrying the protonated A38H$^+$.

The conformation of S-turns bearing the protonated A38H$^+$ were well preserved in all MD simulations (Figure 6, see Supporting Information for the behavior of S-turn backbone torsions). Thus we suggest that a tight and stable A38H$^+$···G+1 BPh contact (Figure 5D) is important for stabilizing (anchoring) the S-turn conformation as well as for proper arrangement of the active site. In contrast, S-turns bearing the canonical A38 shifted away from the scissile phosphate and underwent deformations in most MD simulations (Figure 6), due to the loss of the A38−G+1 4BPh contact (Figures 5B, 5D). It is worth noting that the S-turn region maintained its fold specifically in simulations WT2/G8/A38 and WT/G8/A38/ES, where A38 established instead a hydrogen bond with the A-1(2′-OH) attacking nucleophile, as discussed above. The changes observed in the S-turn region affected also base pairing in helix H4. In particular, the G36 nucleobase often lost its base pair with A26 and became either stacked between residues A26 and C27 or formed a new cis WC base-pair with C27 (displacing the G35 nucleobase) (Supporting Information Figure S5).

Cation Binding Sites. Monovalent cation binding sites identified in the MD simulations presented here in general agree with those determined in previous MD simulations.[23] Ion binding sites of highest Na$^+$ density include two sites within the E-loop (E1 and E2, Figure 7), a site along the major groove of loop A (LA, Figure 7), and a site near the S-turn region (S, Figure 7). These ion binding sites were observed in all simulations regardless of the protonation state of A38. Still, we identified some differences between structures containing either canonical A38 or protonated A38H$^+$ adenine. In particular, expulsion of the canonical A38 from the active site results in opening of the S-turn. Consequently, in simulations with a canonical A38 an additional Na$^+$ ion density appears inside the S-turn, close to the scissile phosphate of the active site (AS spot on Figure 7) in the pocket between the U-2/A-1 sugar−phosphate backbone and the A38 nucleotide. This additional Na$^+$ ion density was detected in the position occupied in the X-ray structures instead by the WC edge of A38. This active site cation density was only observed when the catalytic core was disrupted and opened up toward solvent and therefore did not occur in the two simulations with canonical A38 (WT2/G8/A38, WT/G8/A38/ES) where A38 formed interactions with A-1(2′-OH). When the core remained closed as in the crystal structures, the active site cavity remained inaccessible to cations, as described previously.[8]

Transition of A-RNA Stem to a "Ladder-Like" Structure. It is well established that, while MD simulations of nucleic acids are very insightful, their accuracy is limited by force field approximations, especially on longer simulation time scales.[35,40,49−51] The present simulations reveal one such possible artifact, which, however, does not affect our main conclusions. The A-type helix H4 occasionally formed a distorted structure, named here the "ladder-like" conformation (Figure 8 and Supporting Information Figure S6). Transition of a double helix to the "ladder-like" structure was observed for both force fields (parm99 and parmbsc0) and with different protonation states of A38 and G8, in altogether 4 out of 14 simulations with Na$^+$ counterions (WT/G8t/A38H$^+$, OMe/G8/A38, OMe/G8/A38H$^+$, and WT/G8/A38/bsc0). The "ladder-like" structures were not observed in the two 80 ns excess KCl salt simulations; however, we cannot rule out that such simulations would also provide this artifact. The transition of helix H4 to its "ladder-like" conformation was irreversible at the present time scale (tens to hundreds of nanoseconds). In individual simulations the "laddering" of helix H4 was initiated within the first 30 ns (see Supporting Information Table S4). The "ladder-like" structure was characterized by a shift of the glycosidic χ angle from −160° to ∼−90°, a small decrease in ζ (from ∼−65° to ∼−85°), and an increase of the δ (from ∼80° to ∼110°) and ε (from ∼−160° to ∼−150°) torsions. Sugar puckers of nucleotides in the "ladder-like" structure changed from the initial C3′-endo (A-RNA form) to C2′-exo. The transition was also accompanied by a slight shift of the first peak in the P−P radial distribution function by 0.2 Å toward higher values (see Supporting

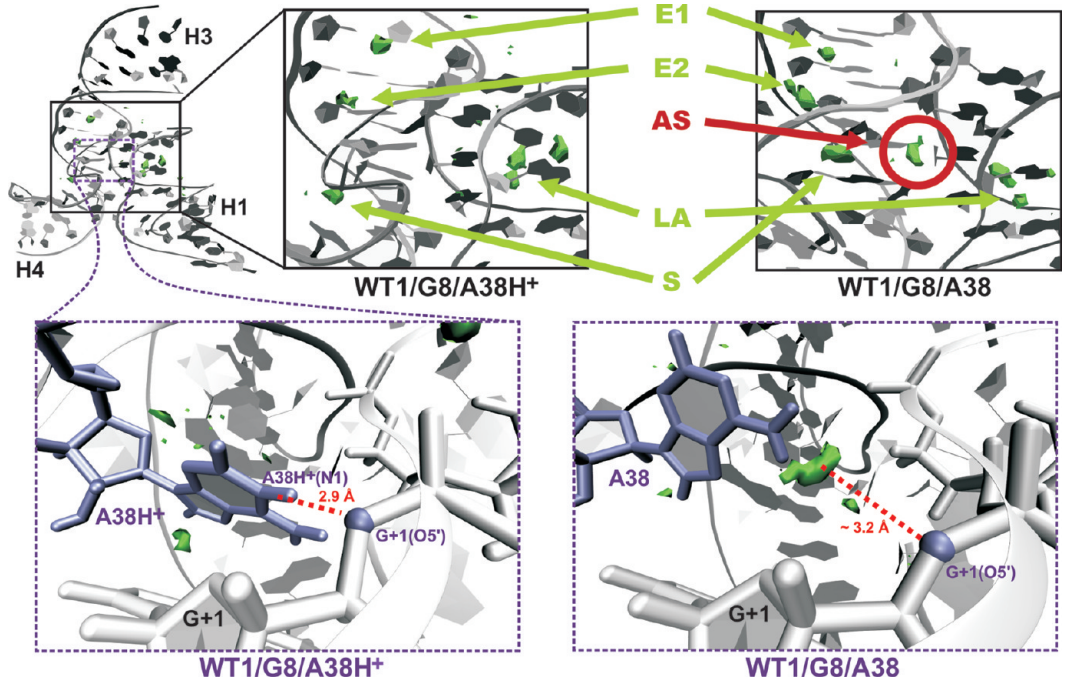

Figure 7. Cation binding sites. Green clouds show regions of high Na^+ ions density. The previously described ion binding sites localized in E-loop (E1 and E2), the major groove of loop A (LA), and close to the S-turn (S) are formed regardless of protonation state of A38. In the case of the WT1/G8/A38 simulation with canonical A38, the shift of the S-turn gives ions access to the active site so that a new density appears (AS, in red circle), approximately at the position of $A38H^+$ in $A38H^+$ bearing simulations (see insets in dashed boxes).

Information Figure S7). Typical signs of the "ladder-like" structure are a loss of the helical twist (rapid decrease from ~33° to ~10°) and an increase in base pair slide (from ~−2 Å to ~4 Å). We can exclude that the formation of this "ladder-like" structure was caused by artificial contacts between replicas under the periodic boundary conditions used in our MD simulations so that it is most likely a force field artifact. Nothing comparable was observed in our recent reference ~50 ns scale A-RNA simulations,[48] our large-scale simulation study of RNA kissing complexes,[52] and numerous other preceding RNA simulation studies. A further investigation of this observation is underway. Importantly, the formation of this distorted helical structure in the distal H4 helix did not affect the conformation of the hairpin ribozyme active site.

Discussion and Conclusions

The hairpin ribozyme is a self-cleaving and -ligating small RNA enzyme that does not require metal ions to achieve catalysis and therefore represents a unique paradigm to study a common mechanism of RNA degradation. Experimental studies have identified two nucleobases essential for acid−base catalysis, G8 and A38, and three plausible reaction mechanisms have been proposed (Figure 2): (i) G8 is deprotonated and acts as a general base accepting a proton from the A-1(2′-OH) group, while A38 plays a structural role and the leaving alcoholate G+1(O5′) is protonated by solvent, (ii) a protonated $A38H^+$ acts as general acid, donating its proton to the leaving alcoholate G+1(O5′), whereas G8 plays a structural role and the A-1(2′-OH) proton is accepted by a solvent molecule or a nonbridging oxygen of the scissile phosphate, (iii) A38 acts as a proton shuttle accepting the proton from A-1(2′-OH) and transferring it to the leaving group G+1(O5′).[23] In addition, a combination of (i) and (ii) where G8 acts as a general base and $A38H^+$ as a general acid can be considered.

The available experimental techniques do not provide sufficient information to unambiguously distinguish which mechanism is dominant or if several microscopic mechanisms are at work under varying conditions, as was recently suggested for the HDV ribozyme.[53] The available crystal structure data provide valuable information about the active site arrangement but are also limited in predictive power due to a medium resolution (~2 Å) and the necessity of using inhibited or mutated structures (e.g., with an A-1(2′-methoxy)) to obtain crystals of a precleavage state. Nonetheless, careful comparison of the available crystal structures with the results of solution biochemical data (such as chemical probing techniques) has established the hairpin ribozyme as a case where both types of data beautifully coincide.[54] Moreover, several independent crystal structures with distinct crystal forms and crystal packing arrangements have been determined and happen to coincide down to the atomic details,[55] providing strong evidence against any influence of the crystalline environment on the structures observed. There are also available NMR structures of hairpin ribozyme isolated domains,[56,57] but both structures change dramatically upon their tertiary structure docking to form the complete ribozyme.[18,58] Unfortunately, no high-resolution NMR structure of hairpin ribozyme in solution exists.[59] One may conclude that the X-ray structures seem to represent well the solution structure of the hairpin ribozyme. In addition, crystal structures present more suitable starting points for MD simulations of RNAs than NMR structures (see ref 40). Classical MD simulations benefit from the fact that they work with the native hairpin ribozyme without any need for chemical modifications to abolish chemistry. They are robust enough to identify those protonation states of nucleobases that are structurally most consistent with X-ray crystallography data.[40] MD simulations also have significant shortcomings due to limited sampling (i.e., relatively short simulation time scales) and the empirical nature of force fields, but when applied wisely, they provide valuable information with unique atomic resolution.[8,12,35,40,42−48,52,60−67]

The presented MD simulations with A-1(2′-methoxy) agree well with crystal structures bearing A-1(2′-methoxy) to prevent

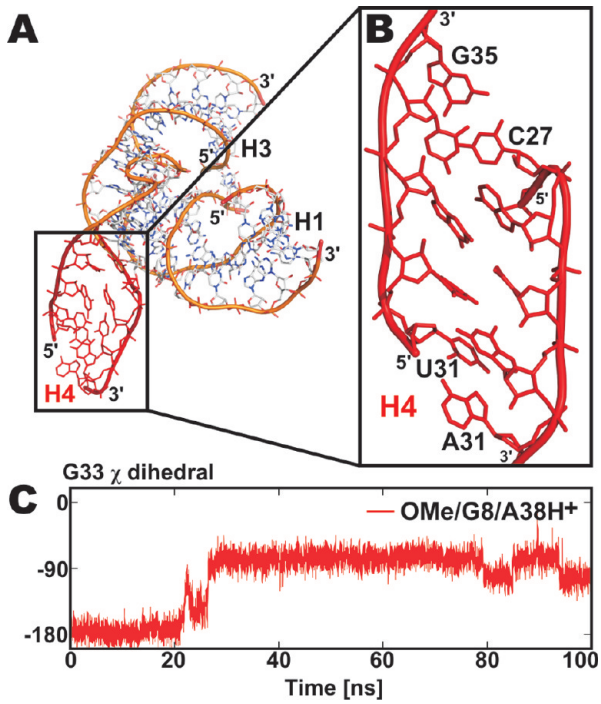

Figure 8. Distortion of the A-type helix H4. (A) A snapshot from the end of the OMe/G8/A38H$^+$ simulation shows a "ladder-like" conformation of helix H4 (red), with a more detailed view in panel (B), which we consider a force field artifact. (C) Time evolution of the glycosidic dihedral χ profile of nucleotide G33 inside the H4 RNA stem during simulation OMe/G8/A38H$^+$. Formation of a "ladder-like" stem structure is accompanied by a shift of χ above $-90°$.

self-cleavage. In contrast, MD simulations with the native A-1(2′-OH) show rapid changes in A-1(2′-OH) group position and A-1 sugar pucker more consistent with the active site architecture observed in crystals bearing a 2′,5′-phosphodiester at the cleavage site.[28] The differences between MD simulations of the hairpin ribozyme with and without a 2′-methoxy group at A-1 explicitly show that the methoxy group distorts the active site. This observation agrees with previous MD simulations, where changes in A-1 sugar pucker and repositioning of its 2′-OH were observed.[8,23] The same changes were also described in a recent crystal structure of a hairpin ribozyme mutant where the native A-1(2′-OH) group was present.[31] This finding clearly implies that mechanistic interpretations based on 2′-methoxy modified RNA structures are not straightforward.

We further observed that the canonical G8 form is structurally consistent with crystallographic data, while the deprotonated G8$^-$ form causes large structural distortions of the active site. The deprotonated G8$^-$ base quickly leaves the active site, likely due to electrostatic repulsion with the scissile phosphate. This observation is not consistent with a catalytic role of G8 as the general base. Similarly, a recent experimental study estimated the pK_a of G8 to 9.5,[20] implying that G8 is largely in the canonical (protonated) form under physiological conditions. In our MD simulations, the G8 enol tautomer remains in contact with the active site and might be considered for a potential structural role in catalysis. However, the ∼19 kcal/mol higher $\Delta G^{\ddagger}$ expected for the self-cleavage in the presence of the G8 tautomeric form (relative to a canonical G8) calls a role for the G8 enol tautomer during catalysis into question.[25] Thus, within the limits of classical MD simulations we suggest that only the canonical G8 is structurally and energetically feasible for the mechanism of self-cleavage. We observed that the G8(N1) imino group of the canonical G8 forms stable hydrogen bonds with the G+1(*pro*-S$_p$) or G+1(*pro*-R$_p$) nonbridging oxygens and/or a hydrogen bond with A-1(O2′). This finding together with prior computational data suggests that G8 likely helps to arrange participating functional groups for catalysis and electrostatically stabilizes the transition states.[23−25]

In contrast to G8, our simulations highlight that the protonated rather than the canonical form of A38 is most consistent with the available crystal structures. Three types of behavior were observed for the unprotonated canonical A38: (i) A38 departs from the scissile phosphate, which leads to large structural changes in the S-turn bearing the A38 base (simulations WT1/G8/A38 and OMe/G8/A38). (ii) A38 retracts from the scissile phosphate but remains at an ∼7 Å distance after losing its base pairing with A24 (simulations WT/G8/A38/bsc0, WT/G8$^-$/A38, and WT/G8t/A38). (iii) A38 establishes a hydrogen bonding contact with A-1(2′-OH) and remains close to the scissile phosphate (simulations WT2/G8/A38 and WT/G8/A38/ES). Once established, the contact between the A-1(2′-OH) nucleophile and the A38 base remains stable until the end of the MD simulation. This contact might be catalytically relevant because A38 was suggested as a potential shuttle capable of accepting a proton from the nucleophile and transferring it to the G+1(O5′) oxygen of the leaving alcoholate.[23] Notably, formation of the A-1(2′-OH)···A38(N1) hydrogen bond is in conflict with the favorable in-line attack angle expected during cleavage, as previously observed,[23] suggesting that proton exchange would have to be followed by a rapid transition of the deprotonated 2′-oxyanion to a position more favorable to in-line attack.

Notably, all simulations with the protonated A38H$^+$ generally agree well with the crystal structure data. Recent Raman spectroscopy analysis yielded direct evidence for an elevated pK_a of A38, suggesting that it can become protonated under physiological conditions.[32] Analysis of the A38 interaction with the scissile phosphate in the crystal structures shows that the corresponding BPh (base-phosphate) interaction does not fall into the classified range of adenine-specific BPh contacts[41] and rather mimics a 4BPh interaction, which is typical only for a guanine nucleobase bearing a protonated N1 nitrogen atom. This may implicate a noncanonical protonation state of A38 to enable this new and rare 4BPh contact. All of these findings suggest that A38 is protonated in the functional hairpin ribozyme. That is, a protonated A38H$^+$ is structurally important to stabilize the reactive fold of the hairpin ribozyme; the S-turn conformation is stabilized by a strong ionic interaction between the scissile phosphate group and the WC edge of the A38H$^+$ nucleobase, which can be classified as a new and rare 4BPh interaction of adenine specific for the N1-protonated adenine.

The protonation of A38 can be also rationalized on the basis of a pocket of very deep negative electrostatic potential (ESP) inside the active site of the hairpin ribozyme,[8,68] which is structurally isolated from solvent cations so that the active site nucleobases are directly exposed to an unsaturated ESP potential.[8] This ESP becomes (partially) saturated by the positive charge of a protonated A38H$^+$. We did not observe penetration of Na$^+$ ions into the closed active site cavity, in agreement with previously published MD simulations.[8,23] Na$^+$ ions enter the active site only in case of a canonical A38, which reconfigures the S-turn and opens the active site to solvent (Figure 7). The entering Na$^+$ ions then take approximately the position of the A38 WC edge to saturate the negative ESP of the cavity. This finding attests to a tendency of the active site to neutralize the deep negative ESP and suggests another role for A38H$^+$, i.e., neutralization of the active site ESP. Conversely, the large negative ESP inside the occluded active site of the hairpin

ribozyme perturbs the pK_a of A38 toward neutrality, as directly observed[69,70] and suggested on the basis of structural data.[31] This represents one of the major differences in utilization of a negative ESP pocket and cations binding between the hairpin and HDV ribozymes.[9,44]

We here also have identified a potential artifact of the AMBER parm99 and parmbsc0 force fields in the formation of a "ladder-like", underwound RNA duplex structure instead of the canonical A-type RNA helix (Figure 8). This "ladder-like" structure appears on a tens-of-nanoseconds time scale and seems to be irreversible on the accessible 50−150 ns time scale. The artifact occurred only in a minority of simulations, affected only the peripheral H4 helix, and did not propagate into the catalytically relevant parts of the simulated structures. However, it clearly appears to have the potential to accumulate in longer MD simulations. Excess KCl salt may slow down or prevent formation of this distorted structure in an A-RNA stem, although more simulations would be needed for validation. A detailed analysis of this behavior is ongoing. We did not notice such a behavior in any of our published RNA studies but detected further cases in unpublished simulations mainly on small RNA model systems. The "ladder-like" helix distortion significantly affects glycosidic χ torsion angles, which leads us to hypothesize that the χ torsion parameters are imbalanced. However, preliminary observations imply that the recently suggested force field with modified χ torsion parameters[71] does not prevent formation of the "ladder-like" structural artifact but may rather speed it up.

Acknowledgment. This study was supported by grants LC512 (to M.O.), LC06030 (to J.Š.), and MSM6198959216 (to M.O.) from the Ministry of Education of the Czech Republic, grants 203/09/1476 (to J.Š.) and 203/09/H046 (to M.O. and J.Š.) from the Grant Agency of the Czech Republic, grants IAA400040802 (to M.O. and J.Š.), KJB400040901 (to J.Š.), and 1QS500040581 (to J.Š.) from the Grant Agency of the Academy of Sciences of the Czech Republic, grants AV0Z50040507 (to J.Š.) and AV0Z50040702 (to J.Š.) from the Academy of Sciences of the Czech Republic, and NIH grant GM62357 (to N.G.W.).

Supporting Information Available: Parameters of nonstandard residues for MD simulations, torsion angles of the S-turn region, evolution of in-line attack angle, and supporting figures. This material is available free of charge via the Internet at http://pubs.acs.org.

References and Notes

(1) Buzayan, J. M.; Hampel, A.; Bruening, G. *Nucleic Acids Res.* **1986**, *14*, 9729.
(2) Buzayan, J. M.; Feldstein, P. A.; Segrelles, C.; Bruening, G. *Nucleic Acids Res.* **1988**, *16*, 4009.
(3) van Tol, H.; Buzayan, J. M.; Feldstein, P. A.; Eckstein, F.; Bruening, G. *Nucleic Acids Res.* **1990**, *18*, 1971.
(4) Walter, N. G.; Burke, J. M. *Curr. Opin. Chem. Biol.* **1998**, *2*, 24.
(5) Fedor, M. J. *J. Mol. Biol.* **2000**, *297*, 269.
(6) Fedor, M. J. *Annu. Rev. Biophys.* **2009**, *38*, 271.
(7) Murray, J. B.; Seyhan, A. A.; Walter, N. G.; Burke, J. M.; Scott, W. G. *Chem. Biol.* **1998**, *5*, 587.
(8) Rhodes, M. M.; Reblova, K.; Sponer, J.; Walter, N. G. *Proc. Natl. Acad. Sci. U.S.A.* **2006**, *103*, 13380.
(9) Krasovska, M. V.; Sefcikova, J.; Reblova, K.; Schneider, B.; Walter, N. G.; Sponer, J. *Biophys. J.* **2006**, *91*, 626.
(10) Krasovska, M. V.; Sefcikova, J.; Spackova, N.; Sponer, J.; Walter, N. G. *J. Mol. Biol.* **2005**, *351*, 731.
(11) Salter, J.; Krucinska, J.; Alam, S.; Grum-Tokars, V.; Wedekind, J. E. *Biochemistry* **2006**, *45*, 686.
(12) Park, H.; Lee, S. *J. Chem. Theory Comput.* **2006**, *2*, 858.
(13) Walter, N. G. *Mol. Cell* **2007**, *28*, 923.
(14) Cochrane, J. C.; Strobel, S. A. *Acc. Chem. Res.* **2008**, *41*, 1027.
(15) Pinard, R.; Hampel, K. J.; Heckman, J. E.; Lambert, D.; Chan, P. A.; Major, F.; Burke, J. M. *EMBO J.* **2001**, *20*, 6434.
(16) Kuzmin, Y. I.; Da Costa, C. P.; Fedor, M. J. *J. Mol. Biol.* **2004**, *340*, 233.
(17) Ditzler, M. A.; Rueda, D.; Mo, J. J.; Hakansson, K.; Walter, N. G. *Nucleic Acids Res.* **2008**, *36*, 7088.
(18) Rupert, P. B.; Ferre-D'Amare, A. R. *Nature* **2001**, *410*, 780.
(19) Rupert, P. B.; Massey, A. P.; Sigurdsson, S. T.; Ferre-D'Amare, A. R. *Science* **2002**, *298*, 1421.
(20) Liu, L.; Cottrell, J. W.; Scott, L. G.; Fedor, M. J. *Nat. Chem. Biol.* **2009**, *5*, 351.
(21) Bevilacqua, P. C.; Brown, T. S.; Nakano, S.; Yajima, R. *Biopolymers* **2004**, *73*, 90.
(22) Lebruska, L. L.; Kuzmine, I. I.; Fedor, M. J. *Chem. Biol.* **2002**, *9*, 465.
(23) Ditzler, M. A.; Sponer, J.; Walter, N. G. *RNA* **2009**, *15*, 560.
(24) Nam, K.; Gao, J. L.; York, D. M. *RNA* **2008**, *14*, 1501.
(25) Nam, K. H.; Gao, J. L.; York, D. M. *J. Am. Chem. Soc.* **2008**, *130*, 4680.
(26) Kuzmin, Y. I.; Da Costa, C. P.; Cottrell, J. W.; Fedor, M. J. *J. Mol. Biol.* **2005**, *349*, 989.
(27) Cottrell, J. W.; Kuzmin, Y. I.; Fedor, M. J. *J. Biol. Chem.* **2007**, *282*, 13498.
(28) Torelli, A. T.; Krucinska, J.; Wedekind, J. E. *RNA* **2007**, *13*, 1052.
(29) Macelrevey, C.; Salter, J. D.; Krucinska, J.; Wedekind, J. E. *RNA* **2008**, *14*, 1600.
(30) Torelli, A. T.; Spitale, R. C.; Krucinska, J.; Wedekind, J. E. *Biochem. Biophys. Res. Commun.* **2008**, *371*, 154.
(31) Spitale, R. C.; Volpini, R.; Heller, M. G.; Krucinska, J.; Cristalli, G.; Wedekind, J. E. *J. Am. Chem. Soc.* **2009**, *131*, 6093.
(32) Guo, M.; Spitale, R. C.; Volpini, R.; Krucinska, J.; Cristalli, G.; Carey, P. R.; Wedekind, J. E. *J. Am. Chem. Soc.* **2009**, *131*, 12908.
(33) Case, D. A.; Darden, T. A.; Cheatham, T. E.; Simmerling, C. L.; Wang, J.; Duke, R. E.; Luo, R.; Merz, K. M.; Pearlman, D. A.; Crowley, M.; Walker, R. C.; Zhang, W.; Wang, B.; Hayik, S.; Roitberg, A.; Seabra, G.; Wong, K. F.; Paesani, F.; Wu, X.; Brozell, S.; Tsui, V.; Gohlke, H.; Yang, L.; Tan, C.; Mongan, J.; Hornak, V.; Cui, G.; Beroza, P.; Mathews, D. H.; Schafmeister, C.; RossW. S., Kollman, P. A. University of California: San Francisco, 2006.
(34) Wang, J. M.; Cieplak, P.; Kollman, P. A. *J. Comput. Chem.* **2000**, *21*, 1049.
(35) Perez, A.; Marchan, I.; Svozil, D.; Sponer, J.; Cheatham, T. E.; Laughton, C. A.; Orozco, M. *Biophys. J.* **2007**, *92*, 3817.
(36) Joung, I. S.; Cheatham, T. E. *J. Phys. Chem. B* **2008**, *112*, 9020.
(37) Cornell, W. D.; Cieplak, P.; Bayly, C. I.; Gould, I. R.; Merz, K. M.; Ferguson, D. M.; Spellmeyer, D. C.; Fox, T.; Caldwell, J. W.; Kollman, P. A. *J. Am. Chem. Soc.* **1995**, *117*, 5179.
(38) Cornell, W. D.; Cieplak, P.; Bayly, C. I.; Kollman, P. A. *J. Am. Chem. Soc.* **1993**, *115*, 9620.
(39) Frisch, M. J., Trucks, G. W.; Schlegel, H. B.; Scuseria, G. E.; Robb, M. A.; Cheeseman, J. R.; Montgomery, J. A., Jr.; Vreven, T.; Kudin, K. N.; Burant, J. C.; Millam, J. M.; Iyengar, S. S.; Tomasi, J.; Barone, V.; Mennucci, B.; Cossi, M.; Scalmani, G.; Rega, N.; Petersson, G. A.; Nakatsuji, H.; Hada, M.; Ehara, M.; Toyota, K.; Fukuda, R.; Hasegawa, J.; Ishida, M.; Nakajima, T.; Honda, Y.; Kitao, O.; Nakai, H.; Klene, M.; Li, X.; Knox, J. E.; Hratchian, H. P.; Cross, J. B.; Bakken, V.; Adamo, C.; Jaramillo, J.; Gomperts, R.; Stratmann, R. E.; Yazyev, O.; Austin, A. J.; Cammi, R.; Pomelli, C.; Ochterski, J. W.; Ayala, P. Y.; Morokuma, K.; Voth, G. A.; Salvador, P.; Dannenberg, J. J.; Zakrzewski, V. G.; Dapprich, S.; Daniels, A. D.; Strain, M. C.; Farkas, O.; Malick, D. K.; Rabuck, A. D.; Raghavachari, K.; Foresman, J. B.; Ortiz, J. V.; Cui, Q.; Baboul, A. G.; Clifford, S.; Cioslowski, J.; Stefanov, B. B.; Liu, G.; Liashenko, A.; Piskorz, P.; Komaromi, I.; Martin, R. L.; Fox, D. J.; Keith, T.; Al-Laham, M. A.; Peng, C. Y.; Nanayakkara, A.; Challacombe, M.; Gill, P. M. W.; Johnson, B.; Chen, W.; Wong, M. W.; Gonzalez, C.; Pople, J. A. *Gaussian 03*; Gaussian, Inc.: Pittsburgh, 2003.
(40) Ditzler, M. A.; Otyepka, M.; Sponer, J.; Walter, N. G. *Acc. Chem. Res.* **2010**, *43*, 40.
(41) Zirbel, C. L.; Sponer, J. E.; Sponer, J.; Stombaugh, J.; Leontis, N. B. *Nucleic Acids Res.* **2009**, *37*, 4898.
(42) Perez, A.; Lankas, F.; Luque, F. J.; Orozco, M. *Nucleic Acids Res.* **2008**, *36*, 2379.
(43) Perez, A.; Luque, F. J.; Orozco, M. *J. Am. Chem. Soc.* **2007**, *129*, 14739.
(44) McDowell, S. E.; Spackova, N.; Sponer, J.; Walter, N. G. *Biopolymers* **2007**, *85*, 169.
(45) Sponer, J.; Spackova, N. *Methods* **2007**, *43*, 278.
(46) Spackova, N.; Sponer, J. *Nucleic Acids Res.* **2006**, *34*, 697.
(47) Reblova, K.; Lankas, F.; Razga, F.; Krasovska, M. V.; Koca, J.; Sponer, J. *Biopolymers* **2006**, *82*, 504.
(48) Besseova, I.; Otyepka, M.; Reblova, K.; Sponer, J. *Phys. Chem. Chem. Phys.* **2009**, *11*, 10701.

(49) Fadrna, E.; Spackova, N.; Stefl, R.; Koca, J.; Cheatham, T. E.; Sponer, J. *Biophys. J.* **2004**, *87*, 227.
(50) Banas, P.; Jurecka, P.; Walter, N. G.; Sponer, J.; Otyepka, M. *Methods* **2009**, *49*, 202.
(51) Fadrna, E.; Spackova, N.; Sarzynska, J.; Koca, J.; Orozco, M.; Cheatham, T. E.; Kulinski, T.; Sponer, J. *J. Chem. Theory Comput.* **2009**, *5*, 2514.
(52) Reblova, K.; Fadrna, E.; Sarzynska, J.; Kulinski, T.; Kulhanek, P.; Ennifar, E.; Koca, J.; Sponer, J. *Biophys. J.* **2007**, *93*, 3932.
(53) Banas, P.; Rulisek, L.; Hanosova, V.; Svozil, D.; Walter, N. G.; Sponer, J.; Otyepka, M. *J. Phys. Chem. B* **2008**, *112*, 11177.
(54) Ryder, S. P.; Strobel, S. A. *Nucleic Acids Res.* **2002**, *30*, 1287.
(55) Alam, S.; Grum-Tokars, V.; Krucinska, J.; Kundracik, M. L.; Wedekind, J. E. *Biochemistry* **2005**, *44*, 14396.
(56) Cai, Z. P.; Tinoco, I. *Biochemistry* **1996**, *35*, 6026.
(57) Butcher, S. E.; Allain, F. H. T.; Feigon, J. *Nat. Struct. Biol.* **1999**, *6*, 212.
(58) Hampel, K. J.; Burke, J. M. *Biochemistry* **2001**, *40*, 3723.
(59) Buck, J.; Li, Y. L.; Richter, C.; Vergne, J.; Maurel, M. C.; Schwalbe, H. *ChemBioChem* **2009**, *10*, 2100.
(60) Auffinger, P.; Hashem, Y. *Curr. Opin. Struct. Biol.* **2007**, *17*, 325.
(61) Orozco, M.; Noy, A.; Perez, A. *Curr. Opin. Struct. Biol.* **2008**, *18*, 185.
(62) Cheatham, T. E. *Curr. Opin. Struct. Biol.* **2004**, *14*, 360.
(63) Mackerell, A. D. *J. Comput. Chem.* **2004**, *25*, 1584.
(64) Hall, K. B. *Curr. Opin. Chem. Biol.* **2008**, *12*, 612.
(65) Chen, A. A.; Draper, D. E.; Pappu, R. V. *J. Mol. Biol.* **2009**, *390*, 805.
(66) Huang, W.; Kim, J.; Jha, S.; Aboul-Ela, F. *Nucleic Acids Res.* **2009**, *37*, 6528.
(67) Romanowska, J.; Setny, P.; Trylska, J. *J. Phys. Chem. B* **2008**, *112*, 15227.
(68) Chin, K.; Sharp, K. A.; Honig, B.; Pyle, A. M. *Nat. Struct. Biol.* **1999**, *6*, 1055.
(69) Tang, C. L.; Alexov, E.; Pyle, A. M.; Honig, B. *Biophys. J.* **2002**, *82*, 131a.
(70) Tang, C. L.; Alexov, E.; Pyle, A. M.; Honig, B. *J. Mol. Biol.* **2007**, *366*, 1475.
(71) Ode, H.; Matsuo, Y.; Neya, S.; Hoshino, T. *J. Comput. Chem.* **2008**, *29*, 2531.
(72) Leontis, N. B.; Westhof, E. *RNA* **2001**, *7*, 499.

JP1001258